

Article

Simulations and Experiments on the Microstructure and Property Evolution of In Situ TiC+Al₃Ti-Reinforced Aluminum Coatings on AZ91D Magnesium Alloy

Liuqing Yang ^{1,2}, Zhiyong Li ^{3,*}, Boqiong Li ^{1,2}, Yingqiao Zhang ³, Shouzheng Wei ³ and Yanlong Jia ⁴

¹ Department of Materials Science and Engineering, Jinzhong University, Jinzhong 030619, China; liuqing891203@163.com (L.Y.); lbq@jzxy.edu.cn (B.L.)

² The Collaborative Innovation Center for the Modified Application of Lightweight Materials, Jinzhong University, Jinzhong 030619, China

³ College of Materials Science and Engineering, North University of China, Taiyuan 030051, China; yingqiaozhang@126.com (Y.Z.); 20150067@nuc.edu.cn (S.W.)

⁴ School of Materials Science and Engineering, Taiyuan University of Science and Technology, Taiyuan 030024, China; b202114310012@stu.tyust.edu.cn

* Correspondence: lizhiyong@nuc.edu.cn; Tel.: +86-035-1392-1809

Abstract: With the development of computational thermodynamics, it is possible to design a material based on its simulated microstructure and properties before practical operations. In order to improve the surface properties of AZ91D magnesium alloy, Jmatpro was used in this study to design an alloy system with in situ TiC+AlTi₃ reinforced aluminum coatings. The Gibbs free energy, hardness, and phase diagrams of aluminum coatings with different ratios of Ti to B₄C were simulated. According to the simulation results, TiB₂, TiC, Al₃Ti₂O₂₂, and Al₄C₃ were formed in the coating while TiB₂, TiC, Al₃Ti₂O₂₂, Al₄C₃, and Al₃Mg₂ were formed in the transition zone between the base metal and the coating. Based on the simulation results, different amounts of Ti were used with B₄C (the ratios were 3:1, 4:1, 5:1, and 6:1) to fabricate TiC+Al₃Ti reinforced aluminum coatings on AZ91D magnesium alloy via laser cladding. The microstructure and phase composition of the coating were studied using scanning electron microscopy (SEM) incorporated with energy-dispersive spectrometry (EDS) and X-ray diffraction (XRD). The results indicated that intermetallic phases, such as AlTi₃(C, N)_{0.6}, AlMg, Al₃Mg₂, Al₃Ti, and TiC were formed in the coatings. As the Ti content increased, the content of Al₃Ti increased and the content of TiC decreased in the coatings, which is consistent with the simulation results. The average hardness of the coatings was approximately four to five times that of the magnesium alloy substrate, and the corrosion current density of the coatings was around 2.5×10^{-6} , which is two orders of magnitude lower than that of AZ91D magnesium alloy.

Keywords: laser cladding; AZ91D magnesium alloy; in situ reaction; JMatPro; TiC



Citation: Yang, L.; Li, Z.; Li, B.; Zhang, Y.; Wei, S.; Jia, Y. Simulations and Experiments on the Microstructure and Property Evolution of In Situ TiC+Al₃Ti-Reinforced Aluminum Coatings on AZ91D Magnesium Alloy. *Crystals* **2023**, *13*, 1151. <https://doi.org/10.3390/cryst13071151>

Academic Editor: Umberto Prisco

Received: 28 June 2023

Revised: 13 July 2023

Accepted: 21 July 2023

Published: 24 July 2023



Copyright: © 2023 by the authors. Licensee MDPI, Basel, Switzerland. This article is an open access article distributed under the terms and conditions of the Creative Commons Attribution (CC BY) license (<https://creativecommons.org/licenses/by/4.0/>).

1. Introduction

As the lightest metal structural material, magnesium alloy has advantages such as high specific strength and stiffness, making it one of the best metals used in the aviation and aerospace fields [1–3]. However, widespread use of magnesium alloy is limited due to its poor wear and corrosion resistance [4–6]. Researchers have tried different approaches to improve the properties of magnesium alloy through surface modification [7–10]. Laser cladding utilizes a precise laser beam to deposit a coating with desired properties on a substrate, and this technique has developed rapidly in recent years owing to its many particular advantages [11–13]. In order to improve the performance of laser-cladded coatings, ceramic particles with high hardness and temperature stability, such as TiC, TiB, and SiC, are often used as the reinforcing phase [14,15]. However, direct addition of ceramic particles to the alloy powder always brings severe cracks due to the thermal expansion difference between the alloy coating and the ceramic particles [16]. Compared to direct

addition of ceramic phases, the in situ synthesis technique forms evenly distributed ceramic particles in the coating via laser cladding, which also has good wetting behavior with the matrix [17]. For example, Savalani M. M. et al. used Ti and carbon nanotube mixed powders to form Ti-based coatings using the in situ synthesis technique [18], and the wear resistance and hardness of the cladding layer increased with an increase in the carbon nanotube content. Y. P. Pu studied the in situ formation of TiN/Ti₃Al, TiC/Ti₃Al, and SiC/Ti₃Al composite coatings using laser cladding on titanium substrate [19].

In order to synthesize in situ ceramic coatings on magnesium alloy, the alloy system must be well designed to make sure the in situ ceramic coatings are successfully generated with the required properties. Furthermore, the morphology of the phases must be carefully controlled, which directly affects the properties of the coatings. Numerical calculation methods and simulation software are widely used by researchers to simulate microstructure. Therefore, an alloy system with a TiC+Al₃Ti reinforced aluminum coating can be designed and the content can be optimized based on the simulated microstructure and properties before practical operations.

The most commonly used numerical calculation methods include deterministic methods, probabilistic methods and phase field methods. Because numerical calculation is always time-consuming and complex, professional software such as Thermo-calc and JMatPro based on the CALPHAD technology have been developed, which are useful for simulating complex multi-component alloy systems. Compared to the Thermo-calc software, the JMatPro software is more intuitive and is widely used to simulate material properties [20,21]. To study the effect of alloy composition, Jooyoung Park et al. simulated the phase transformation and mechanical properties of pore-free samples using JMatPro [22]. Jae-Hyeok Shim et al. calculated the thermodynamics and kinetics of a Fe-0.30C-0.23Si-1.37Mn-0.14V-0.22Cu (in wt%) alloy system using MatCalc and JMatPro software [23].

To improve the surface properties of AZ91D magnesium alloy, the JMatPro software was used in this paper to simulate the phase diagram of aluminum coatings with different (Ti+B₄C) contents. The Gibbs free energy, hardness and phase diagrams of the coatings were simulated and used to predict the phase content in the coatings with different ratios of Ti to B₄C. Furthermore, to verify the simulation results and optimize the performance of the coating, different amounts of Ti were used with B₄C and Y₂O₃ to control the morphology of the phases in the in situ Al-TiC-Al₃Ti composite coating. The effect of Ti on the morphology of in situ generated TiC and Al₃Ti phases was then investigated.

2. Simulation

According to the thermodynamic principle, minimal Gibbs free energy and equal chemical potential are required for ensuring the phase equilibrium of an alloy system. Therefore, the following assumptions can be made:

$$\frac{\partial G_m(\alpha)}{\partial X_i} = \frac{\partial G_m(\beta)}{\partial X_i} \quad (1)$$

$$\mu_i(\alpha) = \mu_i(\beta) \quad (2)$$

Assuming that component *i* exists in the α phase and the β phase, the chemical potentials of *i* in the α phase and the β phase are equal. Unbalanced distribution of *i* will cause phase transitions in the system. By using the CALPHAD technology, it is possible to calculate the molar Gibbs free energy for each phase as shown in Formula (3).

$$G_m = \sum_i X_i G_i^0 + RT \sum_i X_i \ln X_i + \sum_i \sum_j X_i X_j \sum \Omega_V (X_i - X_j)^k \quad (3)$$

Among the thermodynamic terms, G_i^0 is the Gibbs free energy and X_i is the mole fraction of component *i*. The first term represents the overall Gibbs free energy when the

components are simply mixed. The interaction of the components also has an impact on the overall Gibbs free energy, which can be calculated using the last two terms. The second term represents a change in Gibbs free energy caused by the formation of an ideal solution state between the components, in which the particle sizes are supposed to be approximately equal. The third term is the excess free energy caused by the deviation from the ideal solution state.

Based on the above thermodynamic theoretical assumptions, the JMatPro software was used to simulate the phase diagram and properties of the TiC–Al₃Ti reinforced aluminum coatings. The phase diagram was used to design the alloy system and predict the phase formed in the coatings during the laser cladding process.

2.1. Simulation of Coatings with Different (Ti+B₄C) Contents

In order to form in situ TiC–Al₃Ti-reinforced aluminum coatings, Al+(Ti+B₄C) mixed powder was designed and used for laser cladding. According to the reaction formula “5Ti+B₄C→TiC+4TiB”, the ratio of Ti to B₄C was tentatively set as 5:1. The content of (Ti+B₄C) powder decides the amount and morphology of TiC and Al₃Ti in the coating. Therefore, to optimize the content of (Ti+B₄C), the JMatPro software was used to simulate the phase diagram of the coatings with different contents of (Ti+B₄C).

The phase diagram and the important nodes of the simulation results are shown in Figure 1. The liquid phases containing Al, TiB₂, TiC, Al₃Ti_DO₂₂, and Al₄C₃ are presented in the phase diagram. The important nodes listed in Figure 1 provide detailed information regarding the phase change. The starting temperature of the simulation is 1300 °C and the end temperature is 100 °C. When the temperature is 1300 °C, a liquid phase containing TiB₂ and TiC is found. The content of TiB₂ is constant and the content of TiC decreases gradually when the temperature decreases from 1300 °C to 100 °C. At point L4, the liquid phase decreases gradually and Al₃Ti increases gradually because Al in the liquid phase reacts with Ti to form Al₃Ti. When the temperature reaches 789.66 °C, the liquid phase decreases and the content of Al₃Ti increases suddenly because the TiC decomposes, and excess Ti and C elements react with Al to form Al₃Ti and Al₄C₃. When the temperature is 664.78 °C, the liquid phase begins to solidify to form an aluminum solid phase. The content of Al₃Ti increases gradually between 664.78 °C and 100 °C.

As indicated in Figure 1, with an increase in (Ti+B₄C) content, the contents of TiB₂, TiC, Al₄C₃ and Al₃Ti_DO₂₂ increase gradually. When the content of (Ti+B₄C) is 30%, the contents of Al₃Ti and TiC reach their highest, which are 43.45% and 5.98%, respectively. The formation of a high level of the hard phase will lead to an increase in the brittleness of the coating. Therefore, the content of 25% (Ti+B₄C) was selected for further calculation.

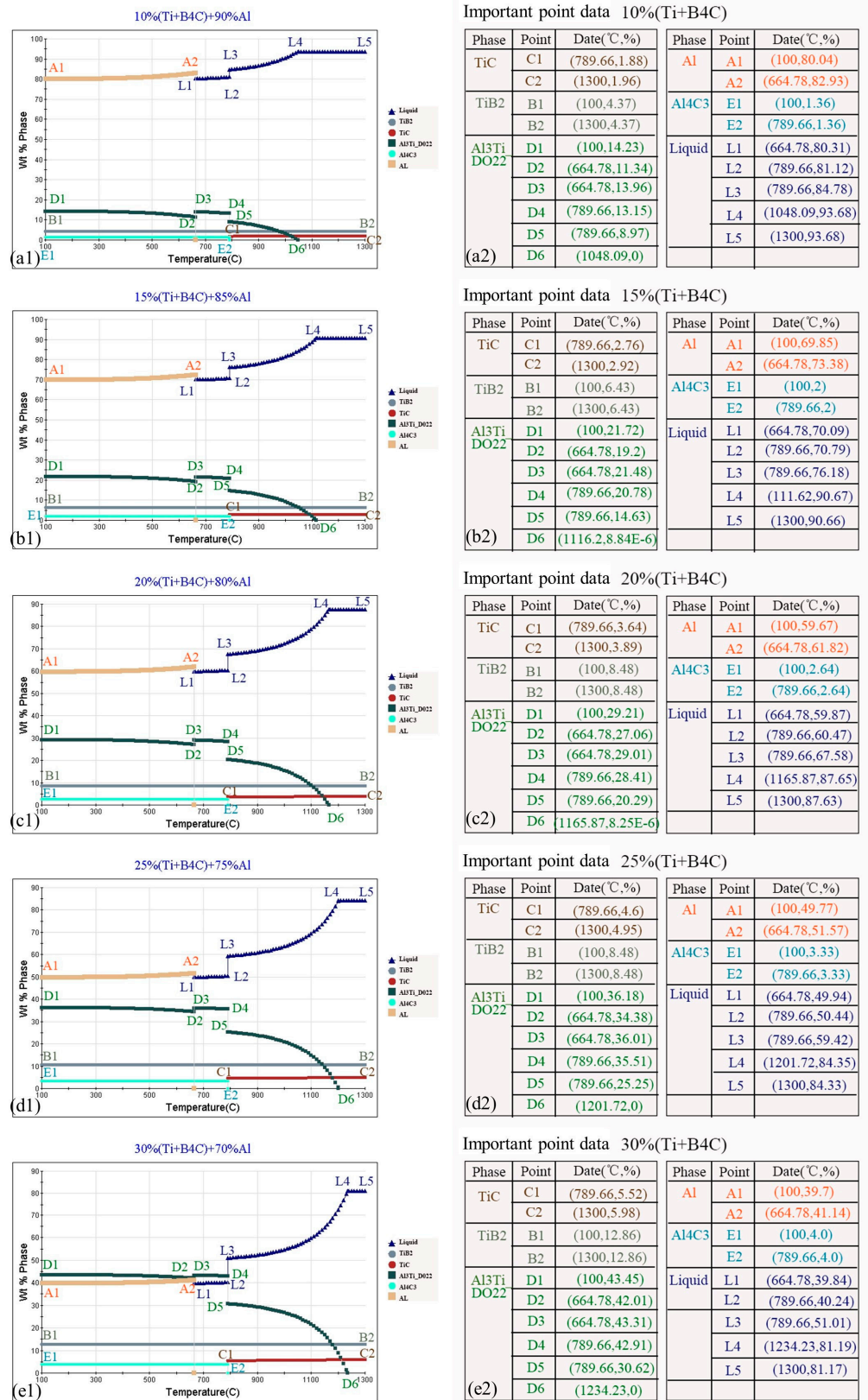
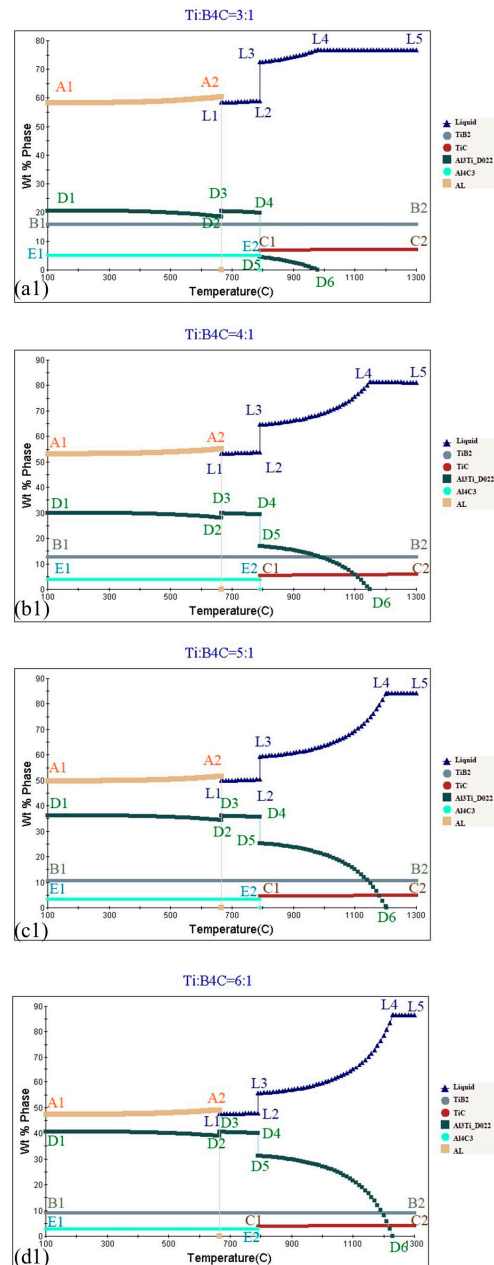


Figure 1. The phase composition diagram with different content of (Ti+B₄C): (a1,a2) 10%(Ti+B₄C); (b1,b2) 15%(Ti+B₄C); (c1,c2) 20%(Ti+B₄C); (d1,d2) 25%(Ti+B₄C); (e1,e2) 30%(Ti+B₄C).

2.2. Simulation of Coatings with Different Ratios of Ti to B₄C

Besides the content of (Ti+B₄C) powder, the ratio of Ti to B₄C also has a significant impact on the performance of coatings. Therefore, as shown in Figure 2, phase diagrams were simulated for the 25% (Ti+B₄C) coatings with different ratios of Ti to B₄C (Ti:B₄C = 3:1, 4:1, 5:1, 6:1). The liquid phase containing TiB₂, TiC, Al₃Ti_DO₂₂, Al₄C₃ and Al is presented in the phase diagram.



Important point data (Ti:B₄C=3:1)

Phase	Point	Date(°C,%)	Phase	Point	Date(°C,%)
TiC	C1	(789.66,6.89)	Al	A1	(100,58.27)
	C2	(1300,7.11)		A2	(664.78,60.37)
TiB ₂	B1	(100,16.07)	Al ₄ C ₃	E1	(100,4.99)
	B2	(1300,16.07)		E2	(789.66,4.99)
Al ₃ Ti DO ₂₂	D1	(100,20.67)	Liquid	L1	(664.78,58.47)
	D2	(664.78,18.56)		L2	(789.66,59.05)
	D3	(664.78,20.47)		L3	(789.66,72.52)
	D4	(789.66,19.88)		L4	(980,76.85)
	D5	(789.66,4.51)		L5	(1300,76.83)
	D6	(979,44.0)			

Important point data (Ti:B₄C=4:1)

Phase	Point	Date(°C,%)	Phase	Point	Date(°C,%)
TiC	C1	(789.66,5.52)	Al	A1	(100,53.16)
	C2	(1300,5.87)		A2	(664.78,55.08)
TiB ₂	B1	(100,12.86)	Al ₄ C ₃	E1	(100,4.0)
	B2	(1300,12.86)		E2	(789.66,4.0)
Al ₃ Ti DO ₂₂	D1	(100,29.99)	Liquid	L1	(664.78,53.34)
	D2	(664.78,28.07)		L2	(789.66,53.88)
	D3	(664.78,29.81)		L3	(789.66,64.65)
	D4	(789.66,29.27)		L4	(1148.23,81.31)
	D5	(789.66,16.98)		L5	(1300,81.28)
	D6	(1148,23, 0)			

Important point data (Ti:B₄C=5:1)

Phase	Point	Date(°C,%)	Phase	Point	Date(°C,%)
TiC	C1	(789.66,4.6)	Al	A1	(100,49.76)
	C2	(1300,4.95)		A2	(664.78,51.55)
TiB ₂	B1	(100,10.71)	Al ₄ C ₃	E1	(100,3.33)
	B2	(1300,10.71)		E2	(789.66,3.33)
Al ₃ Ti DO ₂₂	D1	(100,36.2)	Liquid	L1	(664.78,49.93)
	D2	(664.78,34.4)		L2	(789.66,50.43)
	D3	(664.78,36.03)		L3	(789.66,59.41)
	D4	(789.66,35.53)		L4	(1201.87,84.36)
	D5	(789.66,25.28)		L5	(1300,84.35)
	D6	(1201,87, 0)			

Important point data (Ti:B₄C=6:1)

Phase	Point	Date(°C,%)	Phase	Point	Date(°C,%)
TiC	C1	(789.66,3.94)	Al	A1	(100,47.32)
	C2	(1300,4.27)		A2	(664.78,49.03)
TiB ₂	B1	(100,9.18)	Al ₄ C ₃	E1	(100,2.85)
	B2	(1300,9.18)		E2	(789.66,2.85)
Al ₃ Ti DO ₂₂	D1	(100,40.65)	Liquid	L1	(664.78,47.48)
	D2	(664.78,38.94)		L2	(789.66,47.96)
	D3	(664.78,40.48)		L3	(789.66,55.65)
	D4	(789.66,40.01)		L4	(1229.68,86.57)
	D5	(789.66,31.23)		L5	(1300,86.56)
	D6	(1229.68,2.59E-6)			

Figure 2. The phase diagram with different ratios of Ti to B₄C: (a1,a2) Ti:B₄C = 3:1; (b1,b2) Ti:B₄C = 4:1; (c1,c2) Ti:B₄C = 5:1; (d1,d2) Ti:B₄C = 6:1.

As shown in Figure 2, as the ratio of Ti to B₄C increases, the content of Al decreases gradually when the temperature is 100 °C. As the ratio of Ti to B₄C increases, Al₃Ti_DO₂₂ precipitate at higher temperature and the content of Al₃Ti_DO₂₂ increases gradually. In contrast, the contents of TiB₂, Al₄C₃, and TiC decrease gradually.

2.3. Simulation of Coatings with Consideration of Mg Dilution

The above simulations were carried out on the coatings without considering the effect of the substrate. However, when a magnesium alloy is used as the matrix, the melted Mg substrate can easily diffuse into the coating and a transition zone between the coating and the substrate is formed. To predict the phase formed at the transition zone, the JMatPro software was used to simulate the phase diagrams of the transition zone. The simulation results and the data of the important nodes are shown in Figure 3.

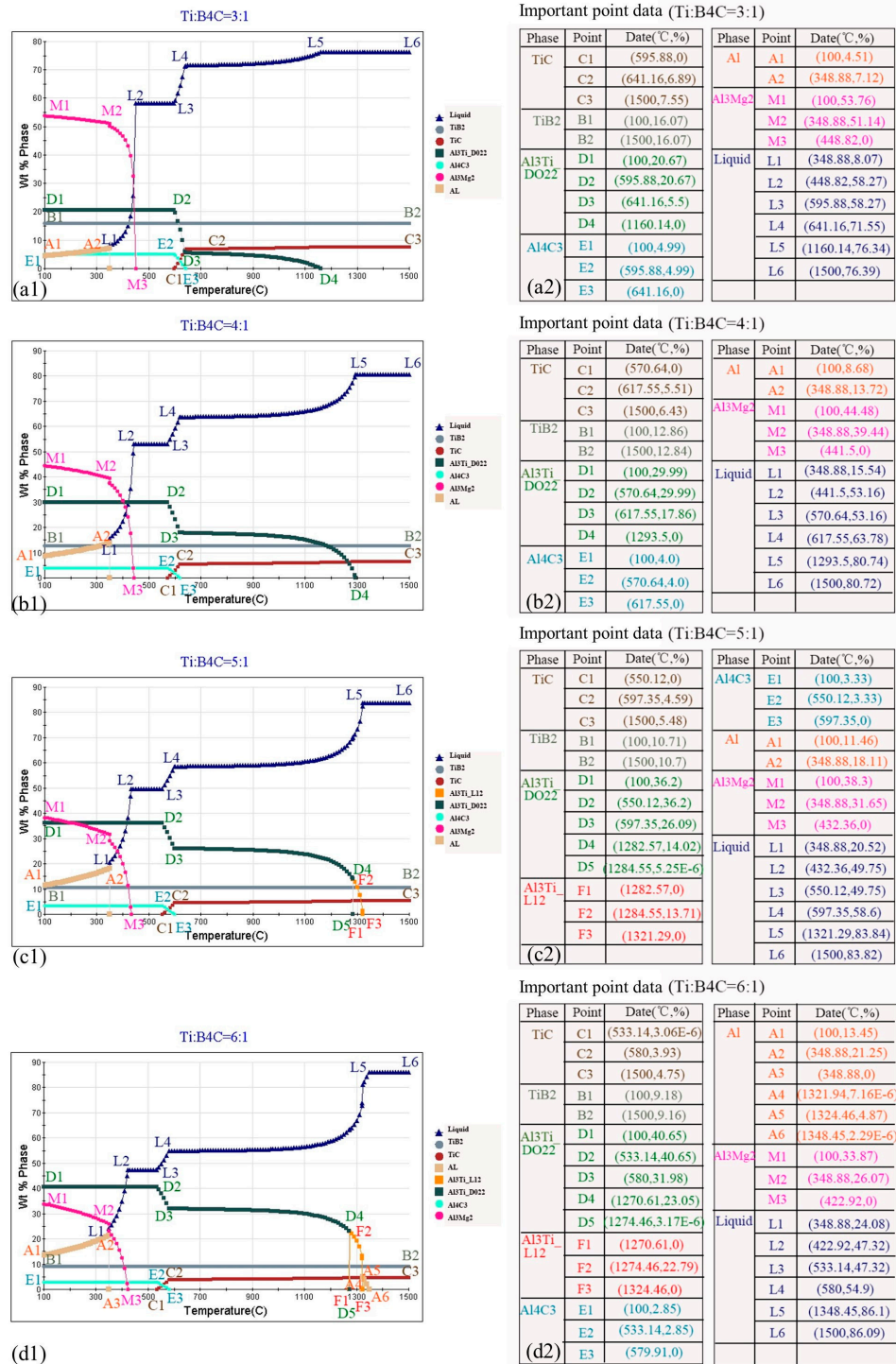


Figure 3. The phase composition diagram of the transition zone: (a1,a2) Ti:B₄C = 3:1; (b1,b2) Ti:B₄C = 4:1; (c1,c2) Ti:B₄C = 5:1; (d1,d2) Ti:B₄C = 6:1.

As shown in Figure 3, a liquid phase containing Al, TiB₂, TiC, Al₃Ti_{DO}₂₂, Al₄C₃, and Al₃Mg₂ is found in the transition zone. Al₃Ti_{L1}₂ is formed when the ratios of Ti to B₄C were 5:1 and 6:1, respectively. The starting temperature of the simulation is 1500 °C and the end temperature is 100 °C. The content of TiC decreases gradually with decreasing temperature. However, the magnitude of the change is not large. When the temperature is lowered at the point L5, the content of the liquid phase begins to decrease. This is because Al in the liquid phase reacts with Ti to form Al₃Ti. As the liquid phase decreases, the content of Al₃Ti gradually increases. The content of TiC in the liquid phase suddenly decreases when the temperature is at point L4. This is because Al in the liquid phase reacts with C and Ti to form Al₄C₃ and Al₃Ti. As the content of TiC in the liquid phase decreases, the contents of Al₃Ti and Al₄C₃ gradually increase. When the temperature reaches the L2 point, the content of the liquid phase is drastically reduced. However, the contents of Al₃Ti, TiB₂, and Al₄C₃ do not change. The reason for the decrease in the content of the liquid phase is that Al and Mg react in the liquid phase to form Al₃Mg₂. The content of Al₃Mg₂ greatly increases as the content of the liquid phase is reduced. The liquid phase disappears until the temperature reaches 348.88 °C. At this time, Al is found. As the Al content decreases, the content of Al₃Mg₂ increases. It is worth noting that Al₃Ti_{L1}₂ is found in the transition phase diagram when the ratios of Ti to B₄C are 5:1 and 6:1. When the ratio of Ti to B₄C is 5:1, the appearance temperature of Al₃Ti_{L1}₂ corresponds to the temperature at which the liquid phase begins to decrease. When the ratio of Ti to B₄C is 6:1, Al first precipitates when the temperature reaches point L5. Al₃Ti_{L1}₂ was found when the temperature reached point A5. Generally, Al₃Ti has a tetragonal DO₂₂ crystal structure with a low symmetry. The L1₂ phase structure is a crystal structure with a higher symmetry than the DO₂₂ structure. It provides more slip system than the DO₂₂ structure. The plasticity of the alloy is improved due to the increase in the slip system. Therefore, the performance of the coatings containing Al₃Ti_{L1}₂ is considered to be better.

Comparing the phase diagrams of the transition zone, the contents of Al₄C₃, TiC, TiB₂ and Al₃Mg₂ decrease gradually with an increase in the ratio of Ti to B₄C. The content of Al₃Ti_{DO}₂₂ gradually increases. Moreover, the disappearance temperature of Al₃Ti_{DO}₂₂ also gradually increases. Al₃Mg₂ is formed in this transition zone. This is because the Mg element in the melted matrix diffuses into the coating to form a compound with the Al element in the coating. Al₃Ti_{L1}₂ is found in the transition phase diagram when the ratios of Ti to B₄C are 5:1 and 6:1. The content of Al₃Ti_{L1}₂ gradually increases with an increase in the ratio of Ti to B₄C. In order to study the cause of the change in phase content in the coating, a thermodynamic simulation was carried out.

2.4. Thermodynamic Simulation

According to the thermodynamic mechanism, the Gibbs free energy is an important parameter which determines the occurrence of a chemical reaction. The chemical reaction can proceed spontaneously when the Gibbs free energy is negative [24]. Otherwise, the reaction cannot proceed spontaneously. The smaller the Gibbs free energy, the greater the thermodynamic driving force for chemical reaction. The JMatPro software was used to simulate the Gibbs free energy of the reaction occurring in the coating, and the results are shown in Figure 4. The Gibbs free energy of all phases becomes smaller with an increase in temperature. That is to say, the reaction spontaneously occurs as the temperature rises. The Gibbs free energy of TiB₂ and Al₄C₃ remains constant as the ratio of Ti to B₄C changes. Al₃Ti disappears at elevated temperatures with an increase in the ratio of Ti to B₄C, which corresponds to the phase diagram. The Gibbs free energy of Al₃Ti decreases while the Gibbs free energy of TiC increases with an increase in the ratio of Ti to B₄C. Therefore, Al₃Ti is easily formed, whereas TiC is less likely to be formed with an increase in the ratio of Ti to B₄C.

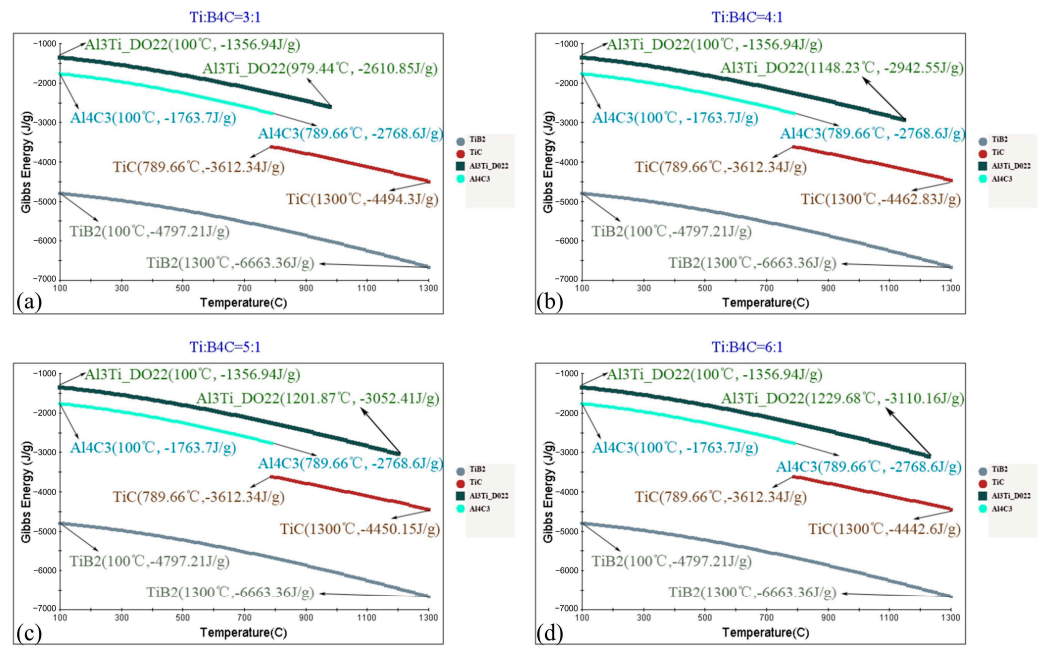


Figure 4. Gibbs free energy of the coating with different Ti and B₄C ratios: (a) Ti:B₄C = 3:1; (b) Ti:B₄C = 4:1; (c) Ti:B₄C = 5:1; (d) Ti:B₄C = 6:1.

Based on the simulation results, the formed phases in situ in the coating can be predicted, and the subsequent reaction is carried out during the laser cladding process.



The simulation results confirm that TiC+Al₃Ti-reinforced aluminum coatings were formed via laser cladding in this study. In the transition zone, Al₃Mg₂ was generated and Al₃Ti_L1₂ was formed when the ratios of Ti to B₄C were 5:1 and 6:1.

2.5. Simulation of Coating Hardness

Hardness is an important indicator of the performance of TiC+Al₃Ti reinforced aluminum coatings. The hardness of the coatings was simulated with consideration of different cooling rates and ratios of Ti to B₄C, and the results are shown in Figure 5. It is clear that the faster cooling rate forms a coating with a higher hardness. With an increase in the ratio of Ti to B₄C, the hardness of the coating decreases gradually.

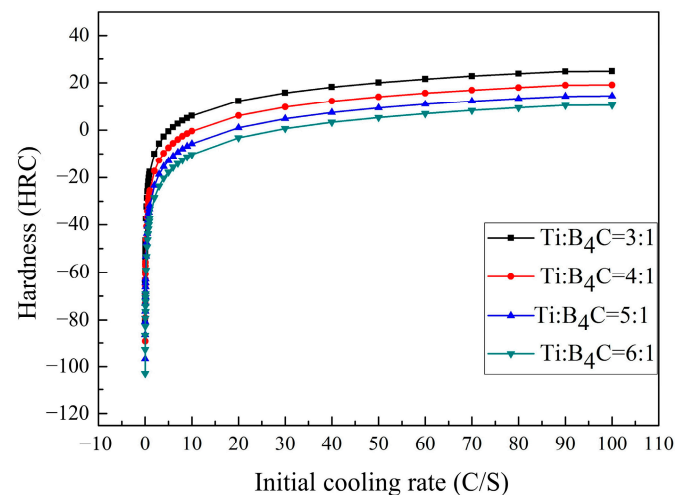


Figure 5. Simulation of coating hardness.

3. Experiments

3.1. Materials and Methods

In order to verify the simulation results and study the properties of the coating, corresponding experiments were performed. The substrate material used in these experiments was the AZ91D magnesium alloy and the dimension of the substrate was 20 mm in length, 15mm in width and 4mm in thickness. The chemical composition of AZ91D magnesium alloy is shown in Table 1. The surface of the substrate was polished using metallographic sandpaper and cleaned using an alcohol solution prior to the experiments.

Table 1. Chemical composition (wt.%) of AZ91D.

Chemical Composition	Mg	Al	Zn	Mn	Si	Be	Others
Relative amount (%)	89.97	8.99	0.71	0.25	0.048	0.0071	≤0.002

Al (99.99% purity, 8 μm), Ti (99.99% purity, 48 μm), B_4C (purity, 3 μm) and Y_2O_3 were selected as the pre-alloyed powders for laser cladding. The weight percentage of the Ti+ B_4C mixed powder was 25%, and the weight percentage of the Y_2O_3 powder was 1.5%. The ratios of Ti to B_4C were 3:1, 4:1, 5:1, and 6:1. The Al+Ti+ B_4C + Y_2O_3 powder was mixed for 40 min in a grinding bowl, and a water glass was used as the binder. The thickness of the pre-coating layer was 0.5 mm.

The laser cladding experiments were carried out using a 0.4 KW pulsed Nd:YAG laser with a beam diameter of 1 mm. The parameters of the laser are shown in Table 2. Ar with a gas flow of 9 L/min was used as a shielding gas during the laser cladding process.

Table 2. The parameters of laser cladding process.

The Parameters	Value
Velocity (mm/min)	150
Pulse width (ms)	4
Current (A)	120
Frequency (HZ)	18
Overlap rate (%)	50

The cross sections of the laser-clad samples were characterized by a JSM-6510 scanning electron microscope incorporated with an energy-dispersive spectrometer (20 kV, WD = 10.0 mm). The microstructural changes in the cross sections of the samples' coatings

were studied. The morphology and quantity of the in situ phase were studied according to the results of scanning electron microscopic analysis. A D/MAX-RB X-ray diffractometer was used to analyze the phase composition of the coating surface. The Cu target was used as the X-ray source with a voltage of 40 kV and a current of 100 mA. Before detection, the unmelted part on the surface of each sample was removed to ensure that only the coated area was left on the surface. The scanning speed was $3^\circ/\text{min}$, and the scanning angle was $20\text{--}80^\circ$. After detection, the phase type of the tested samples' surface was determined by comparing the d value (interplanar spacing) and intensity corresponding to the X-ray diffraction spectrum of the tested sample with data in the PDF card. The microhardness at different distances from the coating surface was tested by a DHV-1000 Vickers microhardness tester under a load of 0.98 N, and the test time was 15 s. For each distance, three points were selected for measurement, and the average value of these three points was taken as the final hardness value. The corrosion potential, corrosion current density, and polarization curve were detected in 1.5% NaCl solution using a rst 5200 electrochemical workstation.

3.2. Phase Analysis

The X-ray diffraction pattern of the coatings with different ratios of Ti and B_4C is shown in Figure 6. The phases in the coatings with different amounts of Ti powder were similar, and $AlTi_3(C,N)_{0.6}$, Al_3Mg_2 , Al_3Ti , TiC, YB_4 , Al_3Y , and AlMg were found in the coatings.

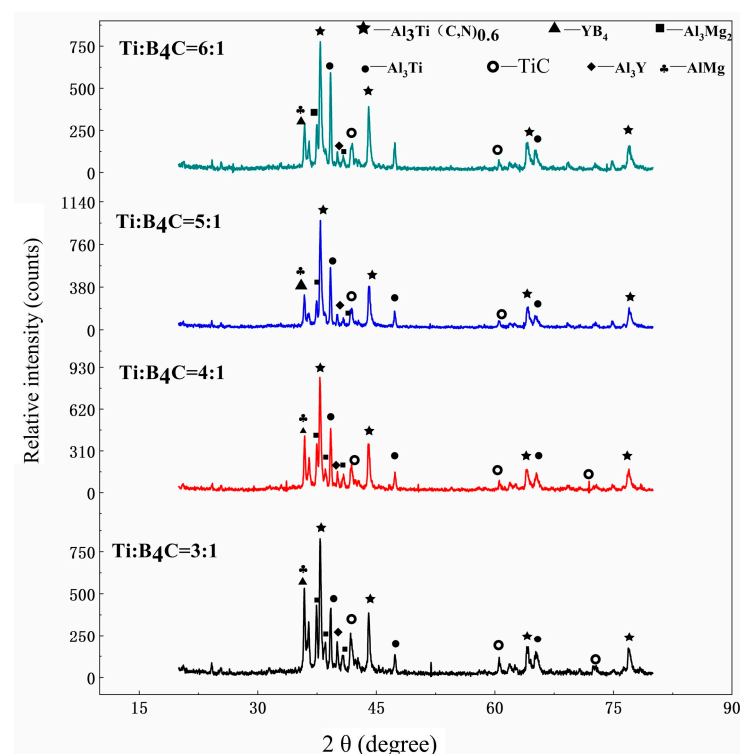


Figure 6. X-ray diffraction spectrum of laser claddings with different ratios of Ti and B_4C .

During laser cladding, the pre-alloyed powders were melted and B_4C particles were decomposed into B and C elements, which rapidly diffused with the stirring of the molten pool. Since Ti is a strong carbide-forming element, the decomposed C elements reacted with Ti to form a TiC ceramic phase. The Y elements from Y_2O_3 reacted with Al to form Al_3Y . Since there is no Y element in the Al alloy module in the JMatPro software, the Y element does not appear in the simulation results. An Al_3Ti strengthening phase was also formed in the coating through the chemical reaction between Al and Ti elements. A small amount of the matrix was melted into the coating and reacted with Al to form Al–Mg

compounds. This is consistent with the simulation results of the transition zone. As shown in Figure 6, the intensity of Al_3Ti increases gradually as the ratio of Ti to B_4C increases from 3:1 to 6:1. In contrast, the intensity of the TiC ceramic phase is basically the same in coatings with different Ti contents. This is consistent with the simulation results. Therefore, as the Ti content in the mixed powder increases and more Ti reacts with Al to form an Al_3Ti hard phase. The presence of Al_3Ti and TiC improves the hardness and wear resistance of the coatings. However, excessive hard phases will increase the crack tendency of the coating [25], which may reduce the overall performance of coatings. The morphology of the hard phase in the coatings also has a great influence on the properties of the coatings. When comparing the X-ray diffraction pattern and the simulation results, it could be observed that TiB_2 was not present in the coatings. This is because a large amount of Ti elements was used to form TiC, Al_3Ti , and $\text{AlTi}_3(\text{C}, \text{N})_{0.6}$. The decomposed B elements reacted with Y to form YB_4 . In the process of laser cladding, the B elements might evaporate. As a result, the B elements were not detected by X-ray diffraction.

3.3. Microstructure

The microstructural images and elemental distribution of the coating (Ti: B_4C = 3:1) are shown in Figure 7. Among the subfigures, Figure 7b–d shows the distribution images of the surface elements in Figure 7a. As shown in Figure 7, a crack-free and high standard metallurgical bonded coating is formed. In Figure 7b, the Mg elements are found to diffuse from the substrate to the coating and Mg–Al alloy compounds are formed in the coating.

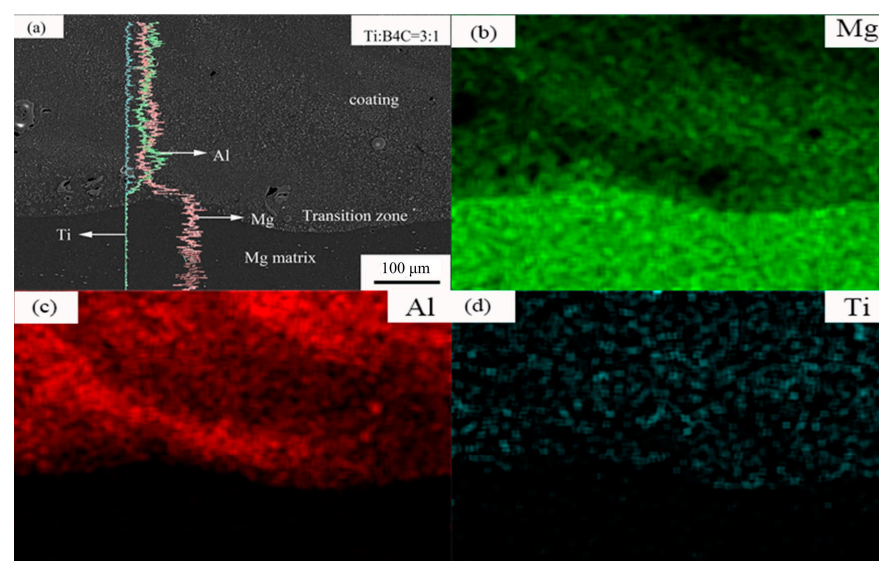


Figure 7. The microstructure image (a) and elemental distributions of Mg (b), Al (c), Ti (d) of the coating (Ti: B_4C = 3:1).

The upper, middle, and lower parts of the coating (Ti: B_4C = 3:1) were magnified for detailed investigation, and the results are shown in Figure 8a,c,e. Figure 8b,d,f show the corresponding element distribution. The distribution of the element content at points 1–5 in Figure 8 is shown in Table 3. Fine particles and phases can be seen in Figure 8, which were caused by the rapid heating and cooling rate of the laser cladding [26], and the growth rate of the generated reinforcing phase was suppressed. Bright white precipitates, gray precipitates and black dotted precipitates were found in the coating. Combined with EDS and XRD results, it could be inferred that the bright white precipitates were TiC ceramic phases (point 1 and point 3), the gray precipitates were Al_3Ti hard phases (point 4 and point 5), and the black spot precipitates were Al–Mg compounds.

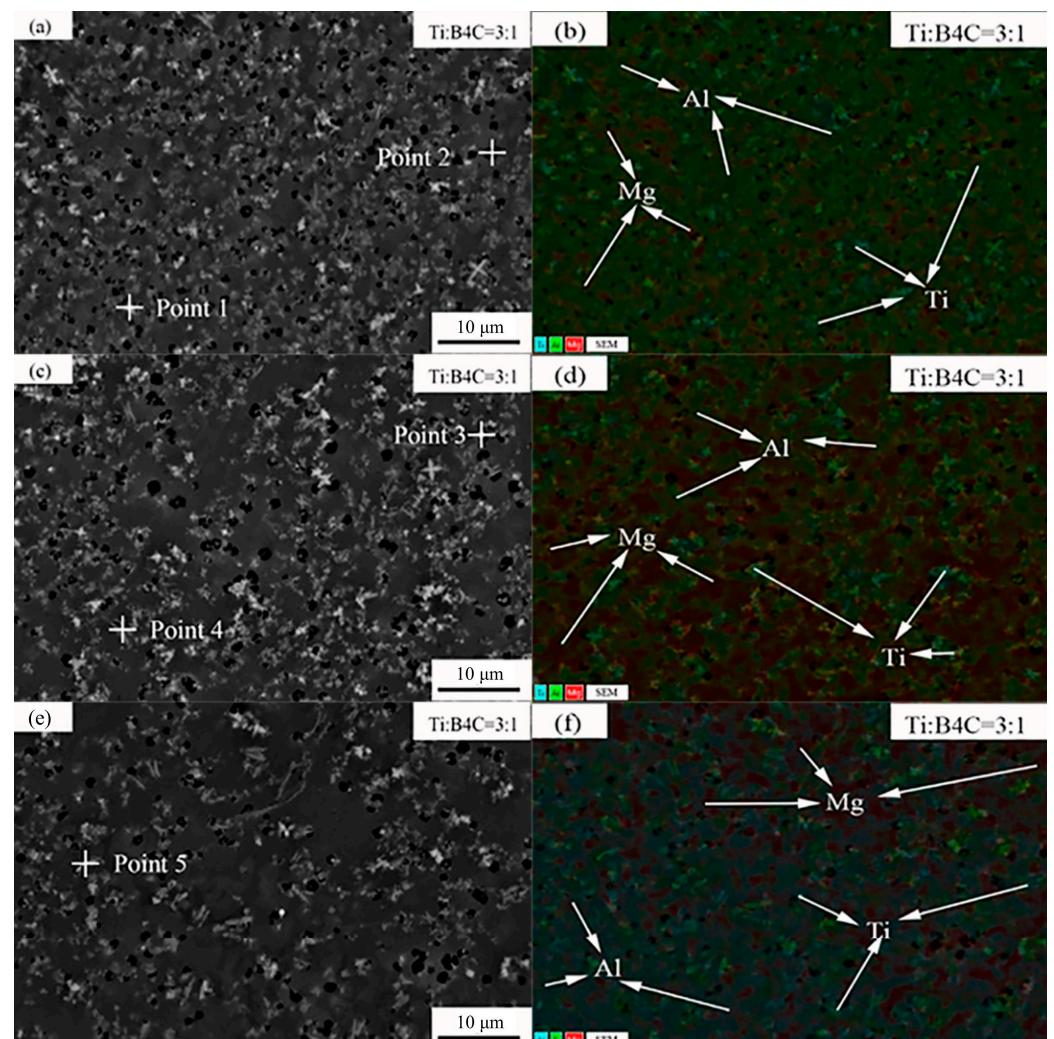


Figure 8. The microstructures of the coating in the (a,b) upper, (c,d) middle, and (e,f) lower parts of the coating (Ti: B₄C = 3:1).

Table 3. Point element content distribution.

Point	Mg	Al	Ti	C	Si	O
1	18.3	28.3	23.2	30.2	-	-
2	32.2	59.9	5.7	-	2.1	-
3	24.8	21.6	24.1	28.5	-	-
4	29.6	23.3	15.1	26.1	0.5	5.4
5	37.5	51.8	9.5	-	1.3	-

When comparing the upper, middle, and lower parts of the coating, the number of precipitates in the coating decreased gradually from the top to the bottom of the cladding layer. The dilution of the cladding layer by the melted base metal caused a graded distribution of the elements, which helped to form the different distribution of precipitates in the coating. The size of the Al₃Ti phases increased gradually from the top to the bottom, which might be caused by the different cooling rates and thermal conductivities in the selected points of the coating [27]. Therefore, at the interface between the coating and the substrate, the number of precipitates decrease and the size of precipitates increase.

The microstructure of the coatings with different Ti contents is shown in Figure 9. As can be observed in Figure 9, the amount of bright white precipitates (TiC) decreases with the

increase in Ti content. The number of gray precipitates (Al_3Ti) increases gradually. This is consistent with the simulation results. According to the Al–Ti binary phase diagram, AlTi_3 metal compounds are formed when the mass fraction of Al atoms ranges from 35% to 51%. AlTi metal compounds are formed when the Al atom mass fraction is in the range of 35% to 51%. Al_3Ti is formed when the Al content is greater than 62% and the temperature drops to 1350 °C. In this study, the Al content in all samples was greater than 62%. Therefore, Al_3Ti was formed. With an increase in the Ti content, more Al_3Ti hard phase was formed. The root cause of this phenomenon is that the Gibbs free energy of Al_3Ti becomes increasingly smaller as the ratio of Ti to B_4C gradually increases. The more negative the Gibbs free energy is, the easier it is to form Al_3Ti . As the ratio of Ti to B_4C increases, the content of C in the coating gradually decreases. This results in insufficient C element in the coating to react with Ti to form TiC. According to the simulation results, the Gibbs free energy of TiC gradually increases with an increase in the ratio of Ti to B_4C . Therefore, the content of TiC is reduced.

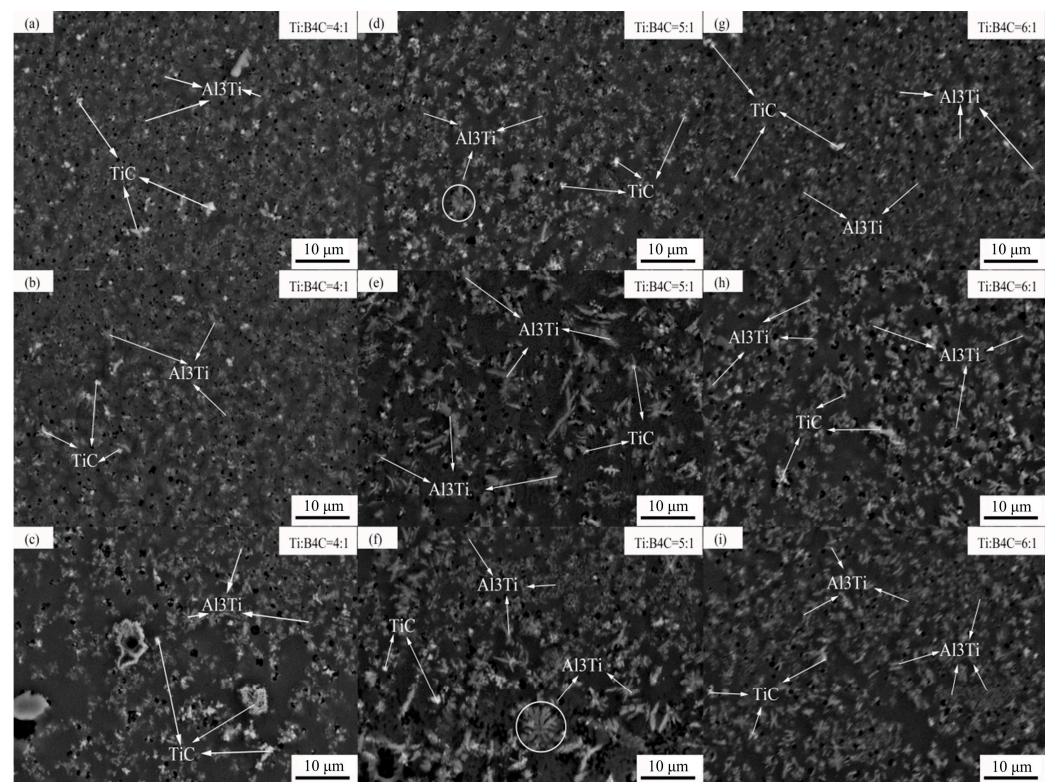


Figure 9. The microstructures of the coatings with Ti: B_4C ratios of 4:1 (a–c), 5:1 (d–f), 6:1 (g–i) in the upper, middle, and lower parts, respectively.

Ti elements in the liquid phase gradually increase when the ratio of Ti to B_4C increases. More Ti elements react with Al to form an Al_3Ti hard phase during laser cladding. The morphology of Al_3Ti in the coating gradually grows from dots to rods. Since Al_3Ti has a DO22-type square crystal structure, it preferentially grows in the direction of the largest density and easily forms rod-like structures. The growth rate of the lattice in the other directions is relatively slow. Al_3Ti rapidly grows in the direction of the maximum density at the tip to form an X-shaped structure. During the experiments, when the ratio of Ti to B_4C was 5:1, the Al_3Ti rod-like structures gathered together to form a petal-like organization. When the ratio of Ti to B_4C was 4:1, a large amount of TiC agglomerated in the lower part of the coating. This led to a serious non-uniform distribution of the hard phase in the coating.

According to the above analysis, it can be concluded that the following chemical reactions occur in the molten bath during laser cladding:



4. Coating Performance Test

4.1. Micro-Hardness

The micro-hardness distribution of the coatings with different ratios of Ti to B_4C is shown in Figure 10. As can be seen from the figure, the hardness of the coatings is much higher than that of the AZ91D magnesium alloy substrate. On the one hand, the microstructure of the coatings is fine due to rapid cooling during the laser processing. This plays a role in grain strengthening. On the other hand, the TiC ceramic phase and Al_3Ti metal compounds were formed in situ in the coatings. The micro-hardness of the coating is increased due to the presence of these hard phases. According to the analysis of the previous simulation results, it can be concluded that the hard phase was formed during the laser cladding process, which greatly improves the hardness of the coating. Compared to the simulation results, higher hardness was measured in the experiment. This is because the hardness value calculated in the simulation is the average hardness of the coatings. The hardness value obtained in the experiment is the average of the hardness of the points.

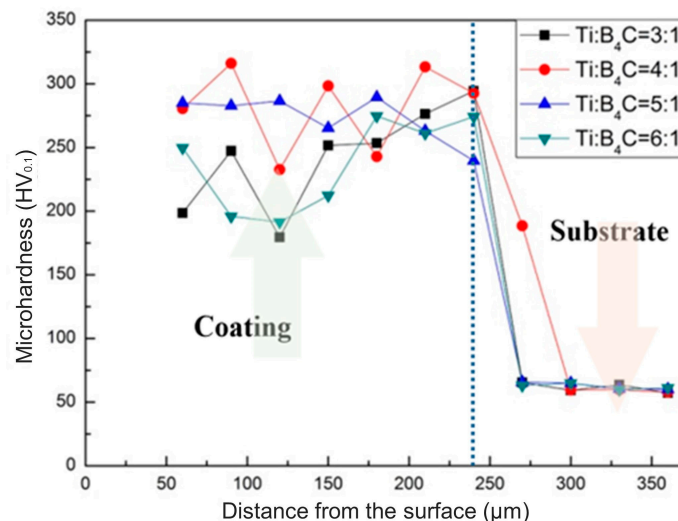


Figure 10. Micro-hardness distribution of coatings.

The distribution of the micro-hardness of the coating was seriously uneven when the ratio of Ti to B_4C was 4:1. The appearance of this phenomenon has a significant relationship with the distribution of the microstructure of the coating. According to the analysis of the microstructure, a large amount of TiC in the in situ ceramic phase agglomerated together when the ratio of Ti to B_4C was 4:1. Obviously, the part where the hard phase was concentrated had higher micro-hardness. This is why the hardness distribution was not uniform. When the ratio of Ti to B_4C was 6:1, the micro-hardness of the coating reduced. Al_3Ti in the coating greatly increased due to the excessive addition of Ti. Al–Ti intermetallic compounds have a large brittleness value at room temperature. Thus, cracks are easily generated during the cooling process. Therefore, the performance of the coating will be reduced due to the excessive generation of Al_3Ti . When the ratio of Ti to B_4C was 5:1, the coating had the highest average hardness (273 HV), which is about 4.6 times higher than that of the magnesium alloy substrate and the distribution of micro-hardness was even.

4.2. Corrosion

The corrosion potentials and corrosion current densities of the coatings with different ratios of Ti to B_4C are shown in Table 4. The polarization curve of the coatings is shown in Figure 11. The results show that the corrosion potentials of the coatings satisfy the following rule: $E_{corr}(AZ91D) < E_{corr}(Ti:B_4C = 4:1) < E_{corr}(Ti:B_4C = 6:1) < E_{corr}(Ti:B_4C = 5:1) < E_{corr}(Ti:B_4C = 3:1)$. The corrosion current densities of the coating satisfy the following rule: $I_{corr}(Ti:B_4C = 3:1) > I_{corr}(Ti:B_4C = 4:1) > I_{corr}(Ti:B_4C = 6:1) > I_{corr}(Ti:B_4C = 5:1)$. It was found that the corrosion resistance of the laser-treated coatings was better than that of the substrate. When the ratio of Ti to B_4C was 5:1, the corrosion potential of the coating was -1.012 V, which is higher than that of the substrate (-1.455 V). The corrosion current density of the coating was 2.501×10^{-6} , which is two orders lower than that of AZ91D. Thus, the corrosion resistance of the coating increased. On the one hand, the corrosion resistance of Al–Mg compounds was better than that of the magnesium alloy substrate. On the other hand, the corrosion potential of the coating increased due to the generation of TiC and Al_3Ti in the coating.

Table 4. Corrosion parameters of different specimens in 1.5% NaCl solution.

Specimen Group	Corrosion Potential (V)	Corrosion Current Density (A/cm^2)
AZ91D	−1.455	1.444×10^{-4}
Ti: B_4C = 3:1	−1.011	1.785203×10^{-4}
Ti: B_4C = 4:1	−1.145	2.389×10^{-5}
Ti: B_4C = 5:1	−1.012	2.501×10^{-6}
Ti: B_4C = 6:1	−1.028	4.596×10^{-6}

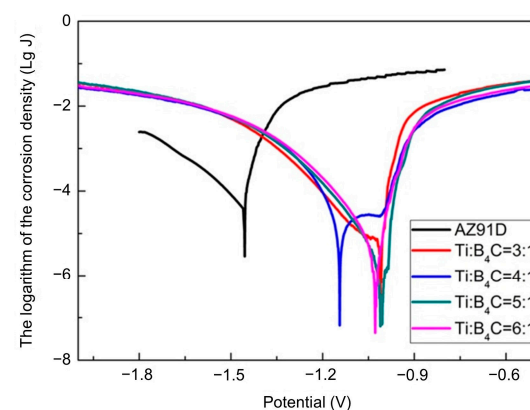


Figure 11. Polarization curve of the coatings.

5. Conclusions

- (1) According to the simulation results, TiB₂, TiC, Al₃Ti₂O₅, Al₄C₃ and Al were formed in the laser-cladded coating while Al, TiB₂, TiC, Al₃Ti₂O₅, Al₄C₃, and Al₃Mg₂ were formed in the transition zone between the coating and the base metal. Al₃Ti₂O₅ was formed in the transition zone when the ratio of Ti to B₄C was 5:1 or 6:1. With an increase in the ratio of Ti to B₄C, the content of Al₃Ti gradually increased. In contrast, the content of TiC gradually decreased.
- (2) An Al–TiC coating was successfully prepared via laser cladding on AZ91D magnesium alloy. A TiC ceramic phase was generated in situ during laser cladding. AlTi₃(C, N)_{0.6}, AlMg, Al₃Mg₂, Al₃Ti, TiC, and Al₃Y were found in the coating. When the ratio of Ti to B₄C was 5:1, the coating had the best performance.
- (3) The hardness of the coating was much higher than that of the AZ91D magnesium alloy substrate. According to the simulation results, the hard phase was generated during the laser cladding process, which greatly improved the performance of the coating. When the ratio of Ti to B₄C was 5:1, the coating had the highest average hardness (273 HV), which is about 4.6 times higher than that of the magnesium alloy substrate.
- (4) The corrosion resistance of the laser-treated coating was better than that of the substrate. When the ratio of Ti to B₄C was 5:1, the corrosion potential of the coating was −1.012 V, which is higher than that of the substrate (−1.455 V). The corrosion current density of the coating was 2.501×10^{-6} , which is two orders lower than that of AZ91D magnesium alloy.

Author Contributions: Conceptualization, L.Y. and Z.L.; software, L.Y. and Y.J.; validation, L.Y.; formal analysis, L.Y.; investigation, L.Y.; data curation, L.Y.; writing—original draft preparation, L.Y.; writing—review and editing, Z.L., B.L., Y.Z. and S.W. All authors have read and agreed to the published version of the manuscript.

Funding: This research was funded by Scientific and Technological Innovation Programs of Higher Education Institutions of Shanxi Province (2022L494); The Collaborative Innovation Center for the modified application of lightweight materials; Shanxi Province Science and Technology Innovation Young Talents Team (202204051001005), Natural Science Research Project of Shanxi Province (202103021224306), Basic Research Program of Shanxi Province (No. 202203021212507), Scientific and technological innovation projects of colleges and universities in Shanxi Province (No. 2022L493).

Data Availability Statement: The raw/processed data required to reproduce these findings cannot be shared at this time as the data also form part of an ongoing study.

Acknowledgments: The work described in this paper was financially supported by The Collaborative Innovation Center for the modified application of lightweight materials; Shanxi Province Science and Technology Innovation Young Talents Team (202204051001005).

Conflicts of Interest: The authors declare no conflict of interest.

References

1. Riquelme, A.; Rodrigo, P. An Introduction on the Laser Cladding Coatings on Magnesium Alloys. *Metals* **2021**, *11*, 1993. [[CrossRef](#)]
2. Istrate, B.; Munteanu, C.; Antoniac, I.V.; Lupescu, S.C. Current Research Studies of Mg-Ca-Zn Biodegradable Alloys Used as Orthopedic Implants-Review. *Crystals* **2022**, *12*, 1468. [[CrossRef](#)]
3. Zhang, Y.Q.; Guo, J.; Xu, G.D.; Li, Z.Y.; Wei, S.Z. Effect of Nd₂O₃ on microstructure, corrosion and wear properties of laser cladding Zr-based amorphous composite coatings on AZ91D magnesium alloy. *Appl. Surf. Sci.* **2023**, *611*, 155587. [[CrossRef](#)]
4. Zhang, Y.Q.; Li, Z.Y.; Liu, S.Y.; Wei, S.Z. Al-WC composite coating on AZ91D Mg alloy by low power pulsed laser cladding. *Kov. Mater.* **2020**, *58*, 169–179. [[CrossRef](#)]
5. Ren, Z.Q.; Zhao, Y.; Han, G.F.; Wang, W.Y.; Zhou, K.B.; He, T.P.; Sun, Y. Laser-Arc Hybrid Cladding of Al-Mg Alloy Coating on AZ80 Mg Alloy: Effect of Laser Beam Oscillations Amplitude. *Materials* **2022**, *15*, 7272. [[CrossRef](#)]
6. Zhang, Y.Q.; Jin, K.; Li, Z.Y.; Wei, S.Z.; Guo, J. Microstructures, Wear and Corrosion Behaviors of Laser Cladding In Situ Synthetic Al₃Ti/AlNi/AlNi₃/MgNi₂ Composite Coatings on Magnesium Alloy using Al as Middle Layer. *J. Mater. Eng. Perform.* **2022**, *32*, 4216–4228. [[CrossRef](#)]

7. Yao, H.; Li, Z.Y.; Zhang, Y.Q.; Wei, S.Z.; Xu, G.D.; Yan, S.; Ren, J.L. Study on laser cladding system of the high-entropy alloy layer on the AZ91D magnesium. *J. Laser Appl.* **2022**, *34*, 032007. [[CrossRef](#)]
8. Li, N.; Wang, Q.; Dong, F.; Liu, X.; Han, P.; Han, Y. Research Progress of Coating Preparation on Light Alloys in Aviation Field: A Review. *Materials* **2022**, *15*, 8535. [[CrossRef](#)]
9. Wan, X.F.; Tian, C.; Li, Y.; Zhou, J.L.; Qian, S.Q.; Su, L.H.; Wang, L. Effect of Y₂O₃ Addition on Microstructure and Properties of Laser Cladded Al-Si Coatings on AZ91D Magnesium Alloy. *Materials* **2023**, *16*, 338. [[CrossRef](#)]
10. Jiang, L.P.; Cui, X.F.; Jin, G.; Tian, H.L.; Tian, Z.M.; Zhang, X.R.; Wan, S.M. Synthesis and microstructure, properties characterization of Ni-Ti-Cu/Cu-Al functionally graded coating on Mg-Li alloy by laser cladding. *Appl. Surf. Sci.* **2022**, *575*, 151645. [[CrossRef](#)]
11. Qi, Z.W.; Chen, C.Y.; Wang, C.Y.; Zhou, Z.K.; Zhou, J.; Long, Y. Effect of different laser wavelengths on laser cladding of pure copper. *Surf. Coat. Technol.* **2023**, *454*, 129181. [[CrossRef](#)]
12. Baltatu, M.S.; Sandu, A.V.; Nabialek, M.; Vizureanu, P.; Ciobanu, G. Biomimetic Deposition of Hydroxyapatite Layer on Titanium Alloys. *Micromachines* **2021**, *12*, 1447. [[CrossRef](#)] [[PubMed](#)]
13. Liu, Y.Y.; Gao, S.Y.; Zhao, W. Laser cladding of Mg-Zn-Y-Zr alloy using Al with different ratios of micro- and nano-SiC powder. *J. Mater. Sci.* **2020**, *55*, 13270–13293. [[CrossRef](#)]
14. Yue, T.M.; Su, Y.P. Laser cladding of SiC reinforced Zr₆₅Al_{7.5}Ni₁₀Cu_{17.5} amorphous coating on magnesium substrate. *Appl. Surf. Sci.* **2008**, *255*, 1692–1698. [[CrossRef](#)]
15. Carcel, B.; Sampedro, J.; Ruescas, A.; Toneu, X. Corrosion and wear resistance improvement of magnesium alloys by laser cladding with Al-Si. *Phys. Procedia* **2011**, *12*, 353–363. [[CrossRef](#)]
16. Muvvala, G.; Karmakar, D.P.; Nath, A.K. In-process detection of microstructural changes in laser cladding of in-situ Inconel 718/TiC metal matrix composite coating. *J. Alloys Compd.* **2018**, *740*, 545–558. [[CrossRef](#)]
17. Liu, Y.H.; Ding, J.Q.; Qu, W.C.; Su, Y.; Yu, Z.S. Microstructure Evolution of TiC Particles In Situ, Synthesized by Laser Cladding. *Materials* **2017**, *10*, 281. [[CrossRef](#)]
18. Wang, D.G.; Chen, C.Z.; Ma, J.; Zhang, G. In situ synthesis of hydroxyapatite coating by laser cladding. *Colloids Surf. B Biointerfaces* **2008**, *66*, 155–162. [[CrossRef](#)]
19. Li, J.; Luo, X.; Li, G.J. Effect of Y₂O₃ on the sliding wear resistance of TiB/TiC-reinforced composite coatings fabricated by laser cladding. *Wear* **2014**, *310*, 72–82. [[CrossRef](#)]
20. Li, Q.T.; Lei, Y.P.; Fu, H.G. Laser cladding in-situ NbC particle reinforced Fe-based composite coatings with rare earth oxide addition. *Surf. Coat. Technol.* **2014**, *239*, 102–107. [[CrossRef](#)]
21. Savalani, M.M.; Ng, C.C.; Li, Q.H.; Man, H.C. In situ formation of titanium carbide using titanium and carbon-nanotube powders by laser cladding. *Appl. Surf. Sci.* **2012**, *258*, 3173–3177. [[CrossRef](#)]
22. Pu, Y.; Guo, B.; Zhou, J.; Zhang, S.; Zhou, H.; Chen, J. Microstructure and tribological properties of in situ synthesized TiC, TiN, and SiC reinforced Ti₃Al intermetallic matrix composite coatings on pure Ti by laser cladding. *Appl. Surf. Sci.* **2008**, *255*, 2697–2703. [[CrossRef](#)]
23. Yang, L.; Li, Z.; Zhang, Y.; Wei, S.; Liu, F. Al-TiC in situ composite coating fabricated by low power pulsed laser cladding on AZ91D magnesium alloy. *Appl. Surf. Sci.* **2018**, *435*, 1187–1198. [[CrossRef](#)]
24. Prasanthi, T.N.; Sudha, R.C.; Saroja, S. Explosive cladding and post-weld heat treatment of mild steel and titanium. *Mater. Des.* **2016**, *93*, 180–193. [[CrossRef](#)]
25. Rai, A.K.; Trpathy, H.; Hajra, R.N.; Raju, S.; Saroja, S. Thermophysical properties of Ni based super alloy 617. *J. Alloys Compd.* **2016**, *698*, 442–450. [[CrossRef](#)]
26. Park, J.; Lee, S.; Kang, S.; Jeon, J.; Lee, S.H.; Kim, H.K.; Choi, H. Complex effects of alloy composition and porosity on the phase transformations and mechanical properties of powder metallurgy steels. *Powder Technol.* **2015**, *284*, 459–466. [[CrossRef](#)]
27. Shim, J.-H.; Hwang, B.; Lee, M.-G.; Lee, J. “Invited Paper” Computer-aided alloy designs of grade 600 MPa reinforced steel bars for seismic safety based on thermodynamic and kinetic calculations: Overview. *Calphad* **2018**, *62*, 67–74. [[CrossRef](#)]

Disclaimer/Publisher’s Note: The statements, opinions and data contained in all publications are solely those of the individual author(s) and contributor(s) and not of MDPI and/or the editor(s). MDPI and/or the editor(s) disclaim responsibility for any injury to people or property resulting from any ideas, methods, instructions or products referred to in the content.